Experimental and Theoretical Investigations of the Inelastic and Reactive Scattering Dynamics of $O(^3P) + D_2$ †

Donna J. Garton, Amy L. Brunsvold, and Timothy K. Minton*

Department of Chemistry and Biochemistry, Montana State University, Bozeman, Montana 59717

Diego Troya

Department of Chemistry, Virginia Tech, Blacksburg, Virginia 24061

Biswajit Maiti and George C. Schatz*

Department of Chemistry, Northwestern University, Evanston, Illinois 60208-3113

Received: July 22, 2005; In Final Form: August 26, 2005

This paper presents a combined experimental and theoretical study of the dynamics of $O(^3P) + D_2$ collisions, with emphasis on a center-of-mass (c.m.) collision energy of 25 kcal mol^{-1}. The experiments were conducted with a crossed-molecular-beams apparatus, employing a laser detonation source to produce hyperthermal atomic oxygen and mass spectrometric detection to measure the product angular and time-of-flight distributions. The novel beam source, which enabled these experiments to be conducted, contributed unique challenges to the experiments and to the analysis, so the experimental methods and approach to the analysis are discussed in detail. Three different levels of theory were used: (1) quasiclassical trajectories (QCT), (2) time-independent quantum scattering calculations based on high-quality potential surfaces for the two lower-energy triplet states, and (3) trajectory-surface-hopping (TSH) studies that couple the triplet surfaces with the lowest singlet surface using a spin−orbit Hamiltonian derived from ab-initio calculations. The latter calculations explore the importance of intersystem crossing in the dynamics. Both experiment and theory show that inelastically scattered O atoms scatter almost exclusively in the forward direction, with little or no loss of translational energy. For the reaction, $O(^3P) + D_2 \rightarrow OD + D$, the experiment shows that, on average, ∼50% of the available energy goes into product translation and that the OD product angular distributions are largely backward-peaked. These results may be interpreted in light of the QCT and TSH calculations, leading to the conclusion that the reaction occurs mainly on triplet potential energy surfaces with, at most, minor intersystem crossing to a singlet surface. Reaction on either of the two low-lying reactive triplet surfaces proceeds through a rebound mechanism in which the angular distributions are backward-peaked and the product OD is both vibrationally and rotationally excited. The quantum scattering results are in good agreement with QCT calculations, indicating that quantum effects are relatively small for this reaction at a collision energy of 25 kcal mol^{-1}.

I. Introduction

The experimental excitation function (collision energy dependence of the integral reactive cross section) for the $O(^3P) + H_2 \rightarrow OH + H$ reaction was recently measured in a crossed-beams experiment and compared to very accurate quantum reactive scattering calculations.[1] Two important results emerged from this study: (1) negligible intersystem crossing was inferred in the reaction of $O(^3P)$ with H_2 at the collision energies under investigation (up to 23 kcal mol^{-1}), and (2) the hyperthermal beam used for the crossed-beams experiments was determined to contain atomic oxygen almost entirely in the ground $O(^3P)$ state. The absence of $O(^1D)$ in the hyperthermal source of oxygen atoms makes feasible the examination of the dynamics of many $O(^3P)$ reactions at high relative velocities with the confidence that $O(^1D)$ reactions will not interfere. The first system chosen for study was the prototypical hydrogen abstraction reaction, $O(^3P) + D_2 \rightarrow OD + D$, because it can be modeled very accurately by modern theoretical methods. In addition, the OD product from this reaction scatters at higher velocities in the c.m. frame than the OH product from the $O(^3P) + H_2$ reaction (for a given relative velocity of the collision); thus, the kinematics of the $O(^3P) + D_2$ system are more favorable for investigating the dynamics of the $O(^3P)$ + molecular hydrogen reaction. A Newton diagram showing $O(^3P)$ scattering from D_2 inelastically (O) and reactively (OD) is presented in Figure 1.

Although the dynamics of the $O(^3P) + H_2 \rightarrow OH + H$ reaction have been studied in detail theoretically,[2−17] the only previous experimental investigations of the dynamics of this reaction are in our laboratory,[1] where we measured the excitation function, and in the laboratory of Weiner and co-workers,[18] who studied the reaction of $O(^3P)$ with H_2 in the first vibrationally excited state ($v = 1$) by laser-induced fluorescence detection of the OH product. The primary reason for the paucity of data on the dynamics of the $O(^3P) + H_2$ ($v = 0$) reaction is the high relative velocity required to overcome the ∼10 kcal mol^{-1} barrier. Many experiments and calculations have been conducted

† Part of the special issue "William Hase Festschrift".

* Corresponding authors. E-mail: tminton@montana.edu (Minton); schatz@chem.northwestern.edu (Schatz).

10.1021/jp054053k CCC: $33.50
Published on Web 10/11/2005

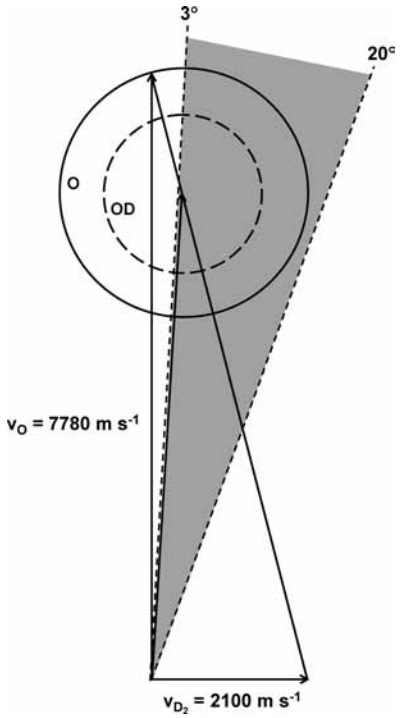

Figure 1. A Newton diagram showing inelastically scattered O and reactively scattered OD from hyperthermal collisions of O(^3P) with D_2 at E_{coll} = 24.8 kcal mol^{-1}. The angular range in gray represents the range of laboratory detection angles used. The circles represent the maximum recoil velocity of the O (solid line) and OD (dashed line) given the energy available for scattering or reaction. The available energy for inelastic scattering is the collision energy, while the available energy for the reaction to form OD is the collision energy minus the endoergicity of the reaction (1.93 kcal mol^{-1}).

on the O(^1D) + H_2 → OH + H reaction, however, which is virtually barrierless.[19−24] These studies have revealed that the OH product angular distribution is forward−backward symmetric, with low vibrational and relatively high rotational excitation of the OH product.[22] At low energies, the reaction occurs mostly on the ground-state surface, ^{1}A′. In contrast, recent calculations on the reaction of O(^3P) with H_2(v,j) have predicted mostly backward-scattering for v = 0 and 1, shifting to more forward-scattering as the initial vibrational energy of the H_2 increases.[25] This shift in scattering behavior has been attributed to the increasing importance of higher impact parameters as the vibrational quantum number increases.[4] The two lowest-lying surfaces, ^{3}A′ and ^{3}A″, are the only triplet surfaces that lead to formation of ground-state OH($^2\Pi$). The third triplet state, 2^3A″, leads only to electronically excited products, which are not energetically accessible in the experiments described herein.

One interesting feature of the O + H_2 potential energy surfaces is the presence of crossings between the low-spin singlet surface and the high-spin triplet surface. Although the singlet surface is much higher in energy on the reagent side (∼45 kcal mol^{-1}), it possesses a deep potential well, causing it to cross the lower-energy triplet surfaces. Hoffmann, Maiti, and Schatz found that the most important singlet−triplet crossings (for nonlinear O−H−H geometries) involve the two low-lying triplet states, ^{3}A′ and ^{3}A″, and the lowest O(^1D) + H_2 surface, ^{1}A′.[26,27] Figure 2 shows potential energy curves along the minimum energy path of the reaction for slightly bent O−H−H geometries.[27] These curves, which are derived from full dimensional potential energy surfaces and CASSCF spin−orbit couplings, show a singlet−triplet crossing just before the top of the triplet barrier. The small energy gap between the singlet and triplet

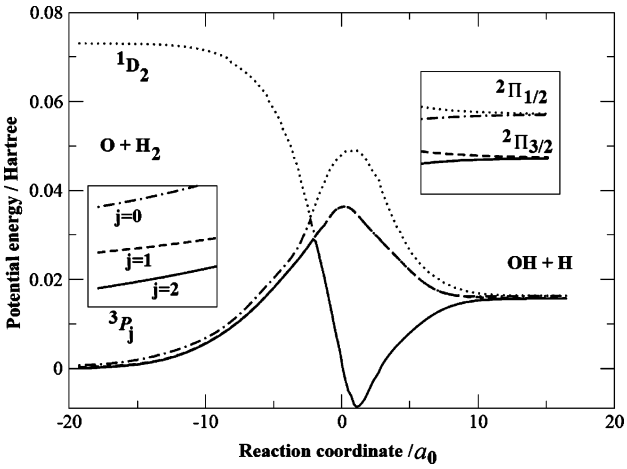

Figure 2. Potential energy curves along the minimum energy path for the triplet reaction with H_2 at slightly bent O−H−H geometries (Jacobi angle of 30°). The surfaces (^{1}A′, ^{3}A′, and ^{3}A″) that correlate to the ground-state OH($^2\Pi$) product and that are involved in intersystem crossing are shown. (The collinear geometry has a lower minimum energy path, but no crossings occur.)

adiabats indicates weak spin−orbit coupling in the system. It therefore appears that intersystem crossing (ISC) from the triplet to the singlet surfaces is possible, although there is no experimental evidence for ISC at collision energies below 23 kcal mol^{-1}. Trajectory-surface-hopping (TSH) studies using the calculated potential surfaces and their couplings indicated that ISC was not important for the reaction close to threshold but that it could contribute as much as 20% to the cross section at collision energies above 20 kcal mol^{-1}. To date, there have been two experimental studies involving O(^3P) reactions in which ISC was observed: (1) Casavecchia et al.[28] saw evidence for ISC in a crossed-beams reactive scattering study of the reaction of O(^3P) with CH_3I, and (2) Naaman and co-workers[29,30] observed evidence for ISC in reactions of O(^3P) with hydrocarbon clusters and organic thin films, wherein insertion of the oxygen atom was observed instead of abstraction. While the first example contained a heavy atom which is believed to facilitate ISC,[28] the second experiment indicated the possibility that ISC can occur without the presence of heavy atoms.

In this paper, the results of crossed-beams experiments are used to explore the dynamics of inelastic scattering of O(^3P) from D_2, as well as the dynamics of the only reactive channel: O(^3P) + D_2 → OD + D. We also present the results of quantum scattering, quasiclassical trajectory (QCT), and TSH studies to interpret the results, including a study of the importance of ISC at high collision energies.

II. Theoretical Details

A. Methods. The quantum scattering and quasiclassical trajectory calculations used the ^{3}A″ and ^{3}A′ potential energy surfaces of Rogers et al.[5] These surfaces are based on high-quality multireference configuration interaction calculations, and in past work[1] we demonstrated that they yield excitation functions near the reactive threshold that are in accurate agreement with experiment. Quantum reactive scattering calculations were carried out using a coupled-channel hyperspherical (CCH) coordinate method as implemented in the ABC quantum scattering program.[31] In these calculations, we have used a maximum hyperradius of 12 au, with a maximum diatomic rotational quantum number (j_{max}) of 30 and a maximum angular momentum projection quantum number (k_{max}) of 20 for all energetically accessible vibrational levels. To obtain con-

TABLE 1: Calculated Global and Vibrational State-Selected Cross Sections[a] (au) for the $O(^3P) + D_2 \rightarrow OD + D$ Reaction

	global	$v = 0$	$v = 1$	$v = 2$	$v = 3$
$E_{coll} = 15$ kcal mol^{-1}					
QCT	0.26 ± 0.02	0.14 ± 0.01	0.12 ± 0.01		
CCH	0.44	0.35	0.09		
$E_{coll} = 20$ kcal mol^{-1}					
QCT	1.63 ± 0.03	0.99 ± 0.02	0.62 ± 0.02	0.02 ± 0.01	
CCH	1.62	1.21	0.40	0.01	
$E_{coll} = 25$ kcal mol^{-1}					
QCT	2.88 ± 0.04	1.84 ± 0.03	0.96 ± 0.02	0.07 ± 0.01	0.01 ± 0.01
CCH	2.88	2.09	0.71	0.08	0.0002

[a] These cross sections are based on $\sigma = (\sigma(^3A'') + \sigma(^3A'))/3$.

verged results up to 25 kcal mol^{-1}, we had to include results using a maximum total angular momentum quantum number (J) of 63. To verify the correctness of the results, we used a wave packet propagation code that is described in ref 25 to determine reaction probability information for a few partial waves, and we obtained results which agreed within a few percent.

The QCT calculations are analogous to those described earlier for $O(^3P) + H_2$.[1] In the present applications, we have run 50 000 trajectories per surface at a collision energy of 25 kcal mol^{-1}, and 25 000 trajectories per surface at collision energies of 20 and 15 kcal mol^{-1}. The time integration step was 2 au, and the cutoff distance for starting and stopping the trajectories was 12 au. For the inelastic scattering calculations, an additional batch of 25 000 trajectories was run for each surface at 25 kcal mol^{-1} using larger impact parameters (up to 8 au).

The TSH calculations use the potential surfaces of Rogers et al., supplemented with a singlet surface from Dobbyn and Knowles[32] and spin−orbit matrix elements from Maiti and Schatz.[27] Details of the calculations are similar to those described by Maiti and Schatz, but in the present application to $O + D_2$ we used 30 000 trajectories for each energy, with an integration time step of 5 au and a cutoff radius of 12 au.

B. Results. Table 1 presents integral cross sections from the CCH and QCT calculations (based on a statistical average over electronic states) for collision energies of 15, 20, and 25 kcal mol^{-1}, including the breakdown of the total cross section into cross sections for the production of OD in different vibrational states. The table shows remarkable agreement between quantum and classical results for the total cross section at the higher collision energies. At the lowest collision energy, the quantum cross section is higher than its classical counterpart, which is consistent with behavior found for $O(^3P) + H_2$. The cross sections for individual product vibrations show less good agreement than the total cross section, with the QCT cross section to the highest allowed vibrational state being systematically higher than its CCH counterpart. This result presumably reflects errors in the assignment of product vibrational states in the QCT calculation as a result of the rounding off of the quantum numbers.

Figure 3 presents stick diagrams of the OD vibration/rotation distributions from the CCH calculations at a collision energy of 25 kcal mol^{-1} as a function of the OD internal energy, showing the results separately for the A″ and A′ surfaces. The contributions from $v' = 0$, 1, and 2 are clearly visible in each figure. The rotational excitation is slightly higher for reaction on the A″ surface than on the A′ surface. This result is a consequence of the larger anisotropy of the A′ surface, which inhibits reactions for bent approaches of O to D_2 to a larger extent than the less anisotropic A″ surface. The results in Figure 3 can be used to determine translational energy distributions. Figure 4 compares CCH and QCT translational energy distributions for reaction on the two surfaces. Here we see that the product translational energy has a maximum at about 13 kcal mol^{-1} for reaction on either of the two surfaces. The CCH and QCT results are in excellent agreement, with the exception of structure in the CCH results that arises from the discrete quantum state structure. Note also that the quantum distribution cuts off at the energy limit, while the classical distribution extends to higher energies as a result of zero-point violation. Fortunately, the error resulting from zero-point violation is minor. Figure 5 shows the CCH and QCT angular distributions for a collision energy of 25 kcal mol^{-1}. Again, we find excellent agreement between quantum and classical results, so in subsequent discussions we consider only the QCT results.

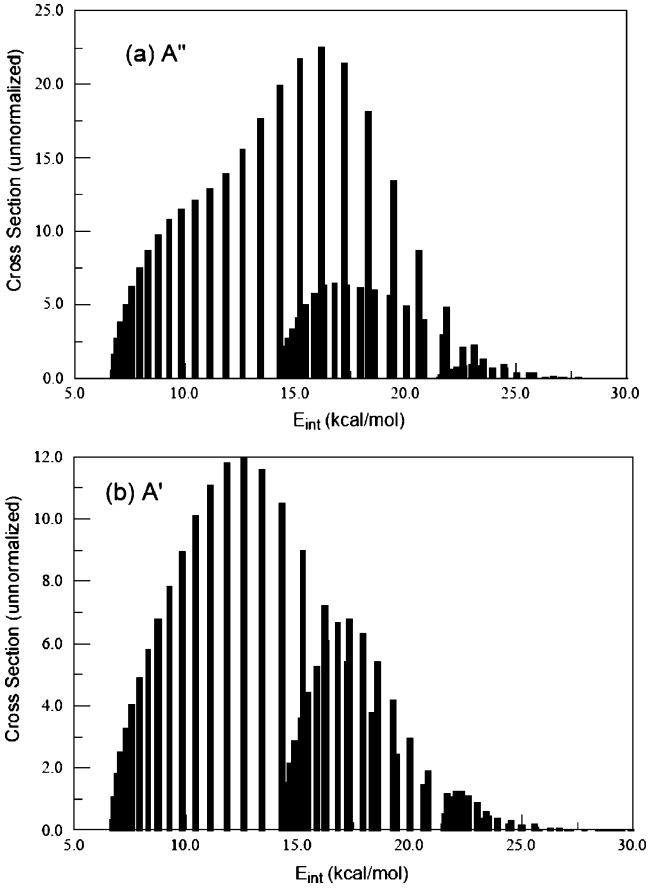

Figure 3. Stick diagram showing the product vibration/rotation distribution from the CCH calculations at 25 kcal mol^{-1} collision energy with (a) presenting results for the A″ potential surface and (b) for A′.

The effect of intersystem crossing on the translational energy and angular distributions is seen in Figure 6, which compares the QCT and TSH results for a collision energy of 25 kcal mol^{-1}. Note that the TSH cross sections are obtained by averaging over the $^3P_2$, $^3P_1$, and $^3P_0$ states of atomic oxygen. The overall integral cross section at this energy is within 10% of the results from

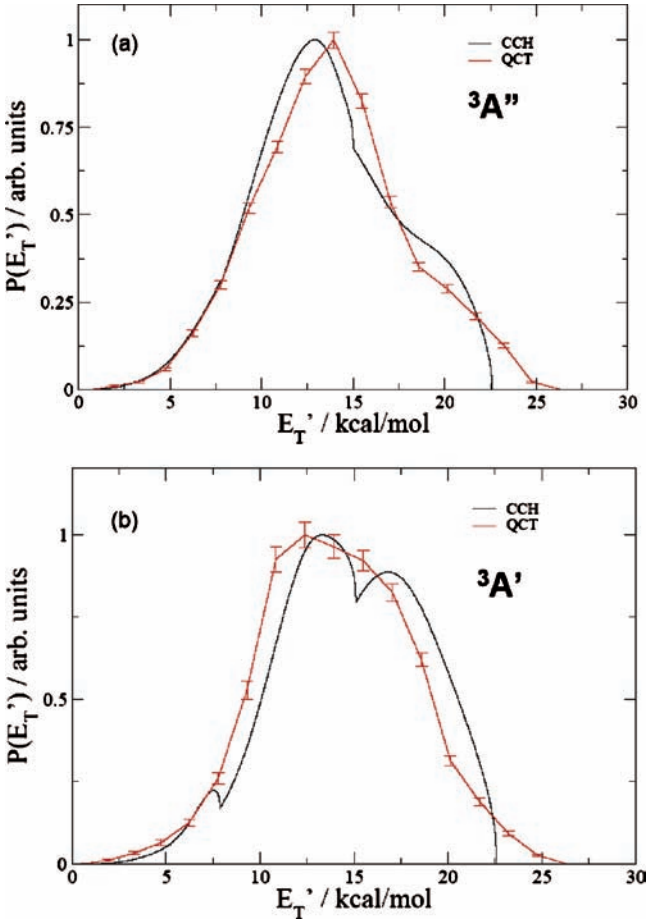

Figure 4. Comparison of CCH and QCT product translational energy distributions for the $O(^3P) + D_2 \rightarrow OD + D$ reaction for $E_{coll} = 25$ kcal mol^{-1} for the (a) A″ and (b) A′ potential energy surfaces.

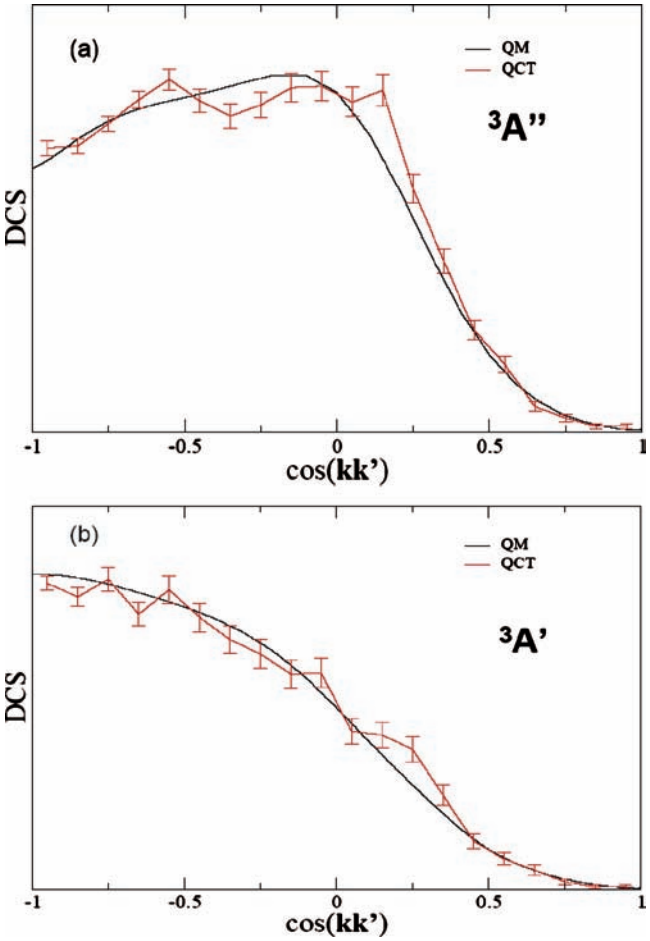

Figure 5. Comparison of CCH and QCT angular distributions for the $O(^3P) + D_2 \rightarrow OD + D$ reaction for $E_{coll} = 25$ kcal mol^{-1} for the (a) A″ and (b) A′ potential energy surfaces.

the QCT or CCH calculations, which is a result that matches the conclusions of Maiti and Schatz,[27] who found that intersystem crossing has a minor effect on overall integral cross sections. Figure 6a shows that the most probable translational energy is the same in the QCT and TSH results, but the low-energy tail of the TSH distribution is more intense. This result is related to a conclusion from the $O + H_2$ studies[27] that intersystem crossing often results in intermediate complex formation characteristic of singlet dynamics, yielding products with more rotational excitation (and hence lower translational energies) than for the triplet-only dynamics. Figure 6b shows that the TSH angular distributions, while still showing predominantly backward-scattering of OD, have a significant forward-scattering component. The presence of forward-scattering in the distributions is the expected result of intermediate complex formation.

III. Experimental Details

A. Methods. The experiments were performed with the use of a crossed-molecular-beams apparatus.[1,33,34] A schematic diagram of the apparatus is shown in Figure 7. Although the crossed-beams technique employed in these experiments is well-known, the high-velocity source of oxygen atoms added significant complexity to the experiments. As this added complexity (coupled with myriad experimental details) severely impacts the data analysis, we discuss here in detail how the experiments were performed.

A pulsed beam of oxygen atoms, produced in a laser detonation source, was crossed at right angles with a pulsed supersonic beam of pure D_2 gas. Products that scattered from the intersection region were detected with a mass spectrometer detector (which rotates in the plane defined by the two beams) as a function of scattering angle and arrival time in the detector. Once ionized by the Brink-type electron-impact ionizer,[35] the products were mass selected with a quadrupole mass filter, counted with the use of a Daly-type ion counter,[36] and accumulated as a function of their arrival time with a multichannel scaler. The number of ions generated in the electron-impact ionizer is dependent on the number density of neutral species present. Therefore, at a particular detector angle and mass-to-charge ratio, the mass spectrometer detector measures number density distributions as a function of arrival time, $N(t)$, which are commonly referred to as time-of-flight (TOF) distributions. Integrated TOF distributions as a function of detector angle or "laboratory angular distributions" are given the designation $N(\Theta)$, where Θ is the angular direction of the scattered products with respect to the direction of the oxygen-atom beam. (The oxygen-atom beam direction is taken to be a laboratory angle of zero, and the positive angular direction is defined by a rotation from the oxygen-atom beam toward the D_2 beam.) The primary data, then, are $N(t)$ and $N(\Theta)$ distributions of mass-selected products. In addition to detecting scattered products, the mass spectrometer detector is used to interrogate the atomic/molecular beams by aligning the detector such that the beam may enter it directly.

The laser detonation source is based on an original design by Physical Sciences, Inc.[37,38] The key elements of this source are a home-built piezoelectric molecular-beam valve,[39] a gold-

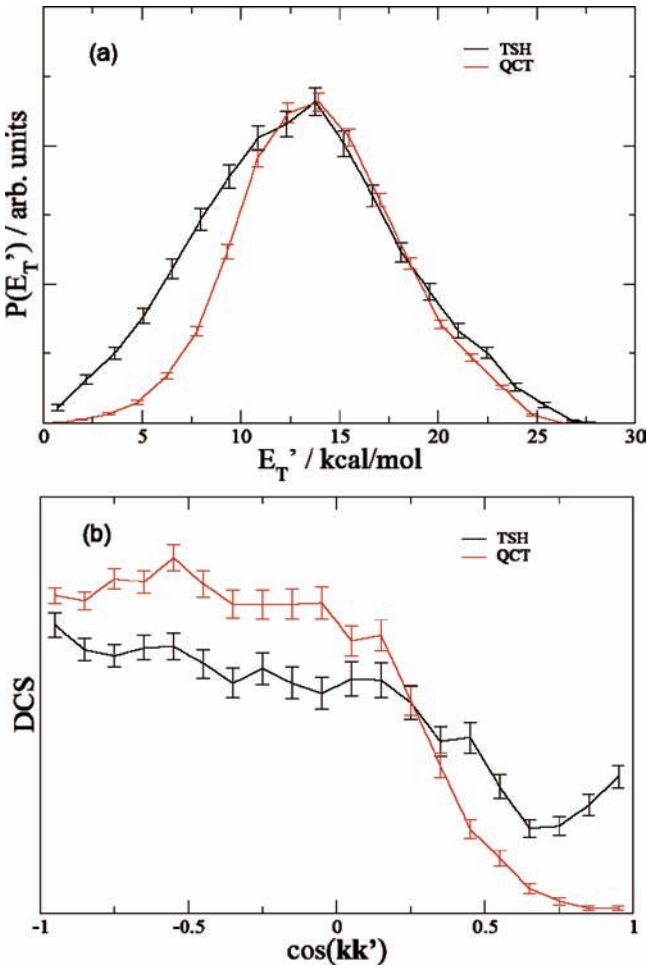

Figure 6. Comparison of QCT and TSH results (averaged over electronic states) for (a) translational energy and (b) angular distributions for the O(^3P) + $D_2 \rightarrow$ OD + D reaction for $E_{coll} = 25$ kcal mol^{-1}.

plated water-cooled copper nozzle, and a high-energy (~7 J pulse^{-1}) CO_2 TEA laser. For the experiments described here, the pulsed valve introduces a high-pressure (18.2 bar stagnation pressure) surge (approximately 100-μs long) of pure O_2 gas into the conical nozzle through a 1-mm diameter × 2.0-mm long cylindrical channel at the apex of the cone. Following a 200−230-μs delay after the pulsed valve is triggered, the CO_2 laser is fired, and the laser light passes through an antireflection-coated ZnSe window into the source chamber where it is then focused into the nozzle with the use of a bare gold mirror of 1-m radius of curvature. The beam waist of the laser is at the apex of the conical nozzle, but as the beam shape is roughly 3 mm × 4 mm at the waist, the laser light mainly impinges on the sides of the gold-coated cone and is reflected down into the orifice channel. The concentrated laser pulse initiates a breakdown of the gas and heats the resulting plasma to more than 20 000 K. The high-temperature, high-density plasma expands rapidly into the 10-cm long, 20° included angle cone following detonation and engulfs the remaining cold gas. The resulting beam pulse contains both atomic and molecular oxygen, traveling at hyperthermal velocities in the range 6−9 km s^{-1}. The ratio of atomic to molecular oxygen is variable, depending on source operating conditions; the atomic fraction used in these experiments was 63%. The oxygen atoms are produced in the ground, or ^3P, electronic state (less than one percent is in the first excited state, ^1D).[1] There may be a small ionic component (≪1%) in the hyperthermal beam, but any residual ions were deflected in a magnetic field produced by permanent magnets mounted on the source chamber roughly 50 cm downstream from the nozzle. The laser detonation source was operated at a repetition rate of 2 Hz, which is the practical limit allowed by the pumping speed of the source chamber. The pressure in the source chamber typically rises to ~1 mTorr during the gas pulse.

The hyperthermal, O-containing beam was first collimated with the use of a 1-cm diameter aperture located 80 cm from the apex of the conical nozzle, and then the beam passed through a region of differential pumping (operating pressure 10^{-6}−10^{-5} Torr) and exited this region through a 1.2-mm diameter skimmer positioned ~96 cm from the apex of the nozzle cone. The hyperthermal beam reached the interaction region (the center of rotation of the detector) 99 cm from the nozzle apex, where it was only negligibly larger than the diameter of the previous skimmer. The operating pressure in the main scattering chamber was ~2×10^{-7} Torr.

The oxygen-atom beam TOF distributions were explored with two detector conditions. Under one condition, the detector was placed directly on the beam axis ($\Theta_{LAB} = 0°$); for the other, the detector was placed 3° off the oxygen-atom beam axis (toward the D_2 beam axis). When the beam was viewed on axis, a small aperture (~125-μm diameter) was used on the front of the detector, while a large square aperture (4 mm × 4 mm) was used on the front of the detector for monitoring the beam off axis. For both on-axis and off-axis configurations, the voltages of the elements of the electron bombardment ionizer were the same. However, for the on-axis configuration, an emission current of 2 mA was used, while for the off-axis configuration, an emission current of 10 mA was used. In addition, the high-voltage electrode of the Daly ion counter was −18 kV for the on-axis configuration and −30 kV for the off-axis configuration. The comparison between beam TOF distributions measured under the two conditions verified that the nominal beam velocity measured under typical conditions used to monitor the beam (on axis) matched the nominal beam velocity measured under the exact detector conditions used to detect scattered products (off-axis conditions). The TOF distribution measured on axis was slightly narrower than the TOF distribution measured off axis. Because the scattering data were collected with the off-axis conditions, we used the off-axis beam TOF distribution in the analysis of the data for inelastic and reactive scattering.

The temporal profile of the atomic oxygen component of the overall hyperthermal beam pulse (collected with the detector viewing the beam directly through a 125-μm diameter aperture) is seen in Figure 8. The dashed line shows the TOF distribution of atomic oxygen, detected at $m/z = 16$. "Time zero" in this figure is the time at which the CO_2 laser fires, which is the point in time when the oxygen atoms are created. The ion flight time has been subtracted, so the observed time is the time required for hyperthermal oxygen atoms to travel 132.7 cm from the apex of the nozzle cone to the electron-impact ionizer. As can be seen by the dashed curve in Figure 8, the overall oxygen-atom pulse is very broad. Because the laser detonation source is essentially a point source, the time (and velocity) width of the oxygen-atom beam pulse can be narrowed with the use of a synchronized chopper wheel, which selects only a small portion of the overall beam pulse. This chopper wheel was placed just past the second aperture, in the main scattering chamber. The chopper wheel had three slots, equally spaced, each 1.5-mm wide and 125-μm thick, and the rotation rate of the chopper wheel was 400 Hz. With careful design of the chopper wheel and drive electronics, including feedback, the chopper wheel was able to run stably for a data collection

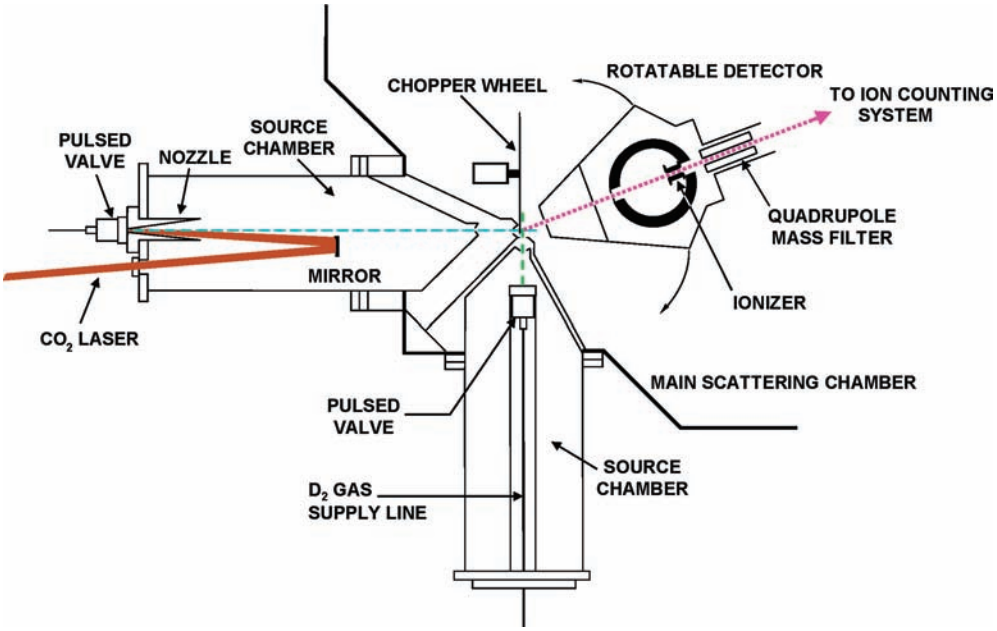

Figure 7. Schematic diagram of the crossed-molecular-beams apparatus.

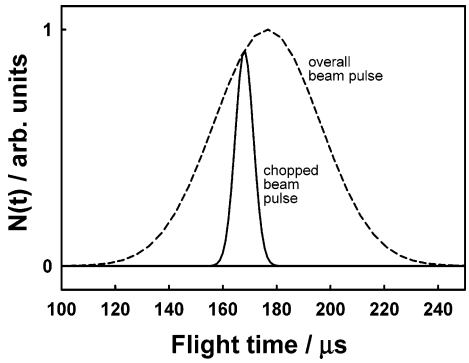

Figure 8. Representative oxygen-atom beam time-of-flight distributions. The overall beam pulse (dashed line) was narrowed with the use of a synchronized chopper wheel (solid line). The synchronization could be varied over the width of the overall pulse in order to tune the nominal oxygen-atom velocity of the selected narrow pulse.

session (1−2 days) with only a ±200-ns variation in its period. The solid curve in Figure 8 represents the narrowed O-atom beam pulse that was selected with the synchronized chopper wheel. Besides defining a narrow oxygen-atom beam pulse, the chopper wheel provided the advantage of blocking all the light from the plasma when the hyperthermal beam was formed.

A piezoelectric pulsed valve, of the same type as that used for the oxygen-atom source, was used to produce a pure beam of D_2. The nozzle orifice diameter was 1 mm, and the pressure behind the orifice was 80 psig. After leaving the nozzle, the D_2 beam passed through a 2-mm diameter skimmer into a differential pumping region and then through a 3-mm diameter aperture into the main scattering chamber, where it crossed the O-atom beam. During the beam pulse, the source chamber reached pressures between 10^{-4} and 10^{-3} Torr, and the differential pumping region reached pressures between 10^{-6} and 10^{-5} Torr. The distance between the nozzle and skimmer was 9.2 cm, and the distance from the skimmer to the 3-mm diameter aperture was 2.8 cm. From this aperture, the beam traveled 1.5 cm to the crossing point of the two beams. The pulse width of the D_2 beam was ∼100 μs—long enough that the duration of the interaction of this beam with the oxygen-atom beam was determined by the temporal width of the oxygen-atom beam, which was less than 15 μs wide (full width at half-maximum) at the interaction region. The velocity of the deuterium beam was found empirically by determining the D_2 velocity that yielded the best circle on a Newton diagram for inelastically scattered O atoms, while keeping the oxygen-atom velocity fixed at its well-known velocity (see below). The velocity of the D_2 beam is probably only accurate to ±10%, but the errors caused by the uncertainty in the D_2 beam velocity are negligible compared to the uncertainties caused by the hyperthermal oxygen-atom beam, which had a nominal velocity that was approximately four times larger than that of D_2 and a velocity spread (full width at half-maximum) that was roughly one-third of that of the D_2 beam velocity.

Timing is important in these crossed-beams experiments, because the two beam pulses must reach the interaction region at the same time in order for reaction between the species in the two reactant beams to occur. The laser detonation source and associated synchronized chopper wheel impose additional complexity on the timing of the experiments. The chopper wheel spins at a constant rate and produces a train of pulses as the slots in the chopper wheel pass over an LED/photodiode arrangement that is displaced by 90° (earlier in time) from the beam axis. The repetition rate of the experiment is determined by a 2-Hz reference oscillator. The train of chopper wheel (photodiode) pulses and the 2-Hz reference pulses are put into a timing circuit that allows the next photodiode pulse following a reference pulse to be output to a digital delay generator capable of producing several pulses with independently adjustable delays. Thus, while the repetition rate is controlled by the 2-Hz reference pulses, the actual experiment timing is controlled by a photodiode pulse from the chopper wheel. The two pulsed beams and the laser are controlled by the delay generator. After the O_2 valve is triggered, there is a delay of about 200−230 μs before the CO_2 laser is fired. The delay between the triggering of the O_2 pulsed valve and the firing of the CO_2 laser is adjusted to provide the desired nominal oxygen-atom beam velocity. The O_2 pulsed valve is triggered at the appropriate time following a photodiode pulse to select the desired portion of the overall oxygen-atom beam pulse with the chopper wheel. The D_2 pulsed valve delay is adjusted to yield the maximum scattered product signal.

The multichannel scaler is typically triggered by the same pulse that triggers the opening of the O_2 pulsed valve; therefore, measured TOF distributions include the laser delay, the flight time of the oxygen-atom beam pulse to the interaction (beam-crossing) region, the flight time of neutral products to the electron-impact ionizer, and the ion flight time from the ionizer to the Daly ion counter. The ion flight time is given by $\alpha(m/z)^{1/2}$, where α, which had a value of 2.44 in these experiments, is a parameter that was determined by comparing the arrival times of the O and O_2 components of the hyperthermal beam. Because the chopper wheel selects only species in the hyperthermal beam that are traveling at a specific velocity, the difference in apparent arrival times of O and O_2 comes from the difference in the ion flight times of O^+ and O_2^+. Thus the ion flight time parameter, α, is found from the measured difference in the O and O_2 arrival times and the difference in the square roots of the mass-to-charge ratios: $\alpha = \Delta t/\Delta(m/z)^{1/2}$. The flight time of the hyperthermal oxygen-atom pulse from the nozzle cone to the interaction region is determined by measuring the velocity of the oxygen-atom beam and calculating the time for the beam pulse to travel the known 99-cm distance to the interaction region. The beam velocity is determined by measuring the oxygen-atom flight time—that is, the time between when the CO_2 laser fires and the time when the beam pulse arrives at the ionizer (132.7 cm away). There is some uncertainty in this measurement, however, because the exact point of origin of the oxygen atoms is not extremely well defined and the pulse width of the laser may be as long as a microsecond (sharp narrow peak of ~100 ns followed by a slow tail). There is thus an estimated (effective) uncertainty in the measured flight times of approximately 2 μs. To conduct the analysis of the scattered products, their TOF distributions must be corrected such that they reflect the number density distributions of products arriving at the ionizer as a function of flight time from the interaction region. The correction is accomplished by subtracting from the raw TOF distributions: the ion flight time, the oxygen-atom flight time from the nozzle to the interaction region, and the delay between the pulsed valve trigger and the firing of the CO_2 laser.

The measured TOF distributions, $N(t)$, and angular distributions, $N(\Theta)$, are number density distributions in the laboratory reference frame, but the relevant microscopic information comes from scattered flux in the center-of-mass (c.m.) reference frame. The two reference frames are different, because the c.m. of the two colliding species is moving in the laboratory frame. The relationship between the c.m. and laboratory velocities can be illustrated with a velocity vector, or Newton, diagram (see Figure 1).[40,41] While a Newton diagram aids in the determination of c.m. velocities and angles from known laboratory velocities and angles, it does not provide a means to determine directly the c.m. translational energy and angular distributions from measured laboratory number density distributions. In fact, because of the complexity of the experiment, including beam velocity distributions, beam angular divergences, ionizer width, and various other apparatus effects, it is extremely difficult (essentially impossible) to deconvolute the measured distributions in order to derive c.m. quantities. Therefore, a "forward-convolution" method is typically employed to derive c.m. quantities from the data. The general approach is to start with trial distributions in the c.m. frame and, taking into account beam velocity distributions and other experimental effects, use a Jacobian coordinate transformation to calculate expected laboratory number density distributions and compare these results with the experimental data. In this method, which has been discussed in detail elsewhere,[42−44] the c.m. scattered flux per unit solid angle, $I_{cm}(E_T, \theta)$, is typically assumed to be separable into the product of two functions: a c.m. translational energy distribution, $P(E_T)$, and a c.m. angular distribution, $T(\theta)$, where E_T is the sum of the translational energies of both products which scatter following a collision in the c.m. frame, and θ is the angle at which a product scatters in the c.m. frame (with respect to the relative velocity vector of approach of the two collision partners). Trial $P(E_T)$ and $T(\theta)$ distributions are used to calculate TOF distributions with the following relationship (derived from the Jacobian transformation):

$$N(t,\Theta) \propto \frac{l^2}{ut^3} I(E_T,\theta) = \frac{l^2}{ut^3} P(E_T) T(\theta)$$

where l is the flight length, u is the product velocity in the c.m. frame, and t is the laboratory flight time from the beam-crossing region to the ionizer. The calculated TOF and angular distributions, which take into account various experimental effects, including the arrival time distribution of the oxygen atoms at the interaction region, are compared with the measured laboratory TOF and angular distributions, and the input $P(E_T)$ and $T(\theta)$ distributions are iteratively adjusted until optimum fits to all laboratory distributions are obtained. Uncertainties in the derived $P(E_T)$ and $T(\theta)$ distributions are determined by observing the maximum variation in these distributions that can still produce reasonable calculated fits. To allow for easy manipulation of the $P(E_T)$ and $T(\theta)$ distributions, parametrized functions are often used. For the analysis of these experiments, a point form for the $P(E_T)$ distribution was sometimes used, and occasionally the $P(E_T)$ distribution was based on the versatile RRK form:[12]

$$P(E_T) = (E_T - B)^p (E_{avail} - E_T)^q$$

where E_{avail} is the total energy available for translation in the c.m. frame. E_{avail} is equal to the sum of the c.m. collision energy, E_{coll}, and the reaction energy, ΔE_r. B, p, and q are adjustable parameters that affect the peak energy and width of the distribution. When approximating the $P(E_T)$ distribution with the RRK form, these parameters are adjusted to give the best fit to the laboratory data. A Legendre polynomial function (varying from six to eleven terms), with adjustable weighting of each of the polynomial terms, was always used to describe the $T(\theta)$ distribution. The Legendre polynomials can be obtained from Rodrigues's formula:

$$T_k(\theta) = \frac{a_k}{2^k k!} \frac{d^k(\cos^2\theta - 1)^k}{d(\cos\theta)^k}$$

where $k = 0, 1, 2, ..., 10$ (for the 11 total polynomial terms used) and a_k represents adjustable parameters. By summing all of the terms, the $T(\theta)$ distribution is obtained. In some cases, a $T(\theta)$ distribution calculated from theory was fit by a Legendre function, and this function was used as an input to the analysis program. In other cases, the parameters in a Legendre function were optimized to provide the best predicted fits to the laboratory TOF and angular distributions. The optimized $T(\theta)$ and $P(E_T)$ distributions can be used to create a c.m. velocity−flux contour map or differential cross section. This contour map is a plot of the scattered flux of a product as a function of angle and velocity in the c.m. frame.

The computer program used to carry out the center-of-mass to laboratory transformation is the MSU XBEAM Program, Version 2.2, which is derived from the CMLAB program that

was originally developed at UC Berkeley in the 1970s and later modified to the GMTHRASH version in the late 1980s and early 1990s. The previous programs were written for crossed-beams experiments with continuous beams, so the MSU XBEAM version required significant modification to account for the crossing of pulsed beams,[45] where one of the beams (the oxygen-atom beam) has a distribution of incident times at the interaction region and the atoms arriving at different times have different velocities. Because the high velocity and the velocity width of the oxygen-atom beam dominated the experimental velocity resolution (see below), the analysis was conducted under the assumption of a monoenergetic D_2 beam.

The crossed-beams method used for these experiments is subject to limitations in velocity resolution. The product velocity in the laboratory frame is the vectorial sum of the velocity of the center of mass of the two colliding species (in the laboratory frame) and the velocity of the reaction product in the c.m. frame. Because the velocity of the center of mass is high ($\sim$6 km s^{-1}), the product velocities are therefore also high. The product velocities are determined by measuring the product flight time over a 33.7-cm distance. Thus, typical flight times are in the range of 30$-$70 μs. Although much care was taken to minimize timing errors in the experiment, the uncertainty in exactly when the CO_2 laser fires and in the width of the laser pulse may lead to errors of as much as 2 μs in the measurement of the flight time, which could create errors in the laboratory velocities of hundreds of meters per second (up to $\sim$10%). Therefore, the uncertainties in translational energies may be between 10 and 20%.

In addition to the uncertainties imparted by the high product velocities, the temporal width of the incident oxygen-atom beam also inhibits velocity resolution and thus the ultimate precision of the derived translational energy distributions. Even with the use of the 400-Hz chopper wheel, the base width of the incident oxygen-atom beam pulse (measured at the detector) was 25 μs, which means that the base width of the product TOF distributions will be at least this much, even if the product translational energy distribution is extremely narrow. The width of the arrival time of the incident beam is accounted for in the analysis, as is the fact that different arrival times correspond to different beam velocities and thus different collision energies. However, when the width of the arrival time distribution accounts for a significant amount of broadening of the product signal, then the energy width of the trial $P(E_T)$ distribution may be varied by a few kcal mol^{-1} and have no significant effect on the calculated TOF distributions. Thus, it becomes difficult to derive a unique $P(E_T)$ distribution. Furthermore, the analysis assumes that over the range of c.m. collision energies resulting from the velocity spread in the oxygen-atom beam, the shape of the $P(E_T)$ distribution of the products remains constant. This approximation breaks down if the shape of the $P(E_T)$ distribution is strongly dependent on collision energy. So, the $P(E_T)$ distribution that is derived represents a sort of average distribution over the range of collision energies in the experiment. In the experiments reported here, it is believed that the width of the arrival time distribution of the incident oxygen-atom beam results in more uncertainty in the derived $P(E_T)$ distributions than does the range of c.m. collision energies.

It is possible to narrow the temporal width of the oxygen-atom beam pulse even further by (1) spinning the chopper wheel faster, (2) reducing the width of the slots in the chopper wheel, or (3) reducing the diameter of the beam as it passes through the chopper wheel. Unfortunately, all of these approaches reduce the beam intensity and thus the signal in the experiment. The beam diameter was made narrow with the use of the 1.2-mm diameter skimmer, and the choice of chopper slot width and wheel speed was investigated. It was found more effective to use a wider slot and spin the wheel faster than to use a narrower slot and spin the wheel slower. A possible reason for this observation is that the incident oxygen-atom beam pulse produces a localized pressure increase in the vicinity of a narrow slot, which leads to multiple collisions and a consequent attenuation of the pulse that makes it through the slot. The local pressure does not build up to this extent if the slot width is larger. Another possibility is that scattering from the edges of the slot (again leading to multiple collisions and beam attenuation) is more important for narrower slots than for wider slots. A slot width of 1.5 mm and a wheel speed of 400 Hz were found to provide a good overall compromise.

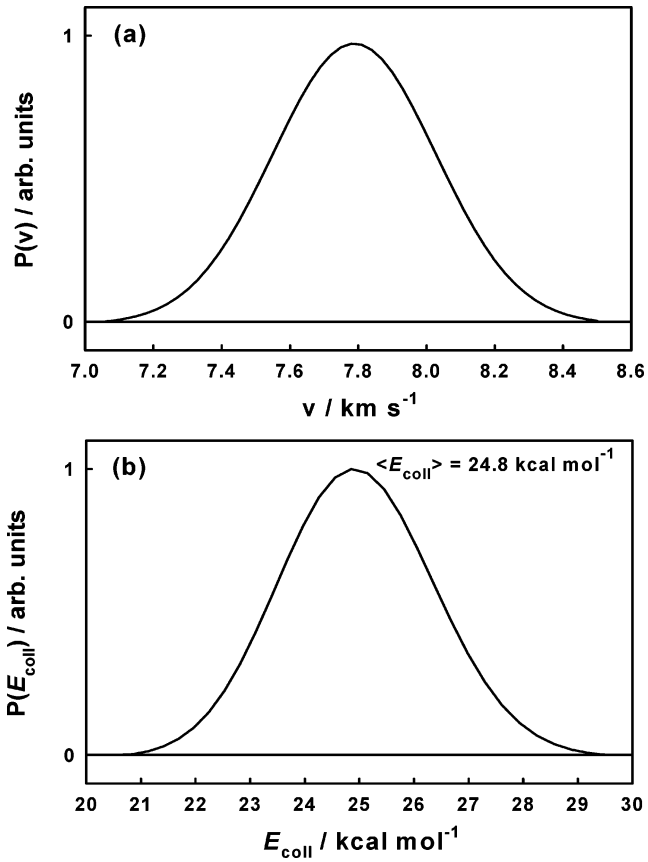

Figure 9. (a) Velocity distribution of the oxygen atoms in the hyperthermal beam used for these experiments. (b) Distribution of collision energies for O(^3P) collisions with D_2, assuming the variability in collision energy arises entirely from the oxygen-atom velocity distribution shown in (a).

Figure 9a shows the oxygen-atom velocity distribution that was selected with the chopper for these experiments. The peak velocity is 7780 m s^{-1}. From this velocity of oxygen atoms and a nominal D_2 velocity of 2100 m s^{-1}, the c.m. collision energy is calculated to be $E_{coll} = 1/2\ \mu v_{rel}^2 = 24.8$ kcal mol^{-1}, where μ is the reduced mass, and v_{rel} is the relative velocity of approach of the two collision partners. The oxygen-atom velocity distribution dominates the c.m. distribution of collision energies, which is shown in Figure 9b, assuming a fixed D_2 beam velocity of 2100 m s^{-1}. This distribution of collision energies should be taken as the narrow limit, as accounting for the width of the D_2 beam velocity distribution would slightly broaden the collision energy distribution.

Inelastic scattering signals were detected at $m/z = 16$ (O^+) and 32 (O_2^+). The range of detector angles for which data were

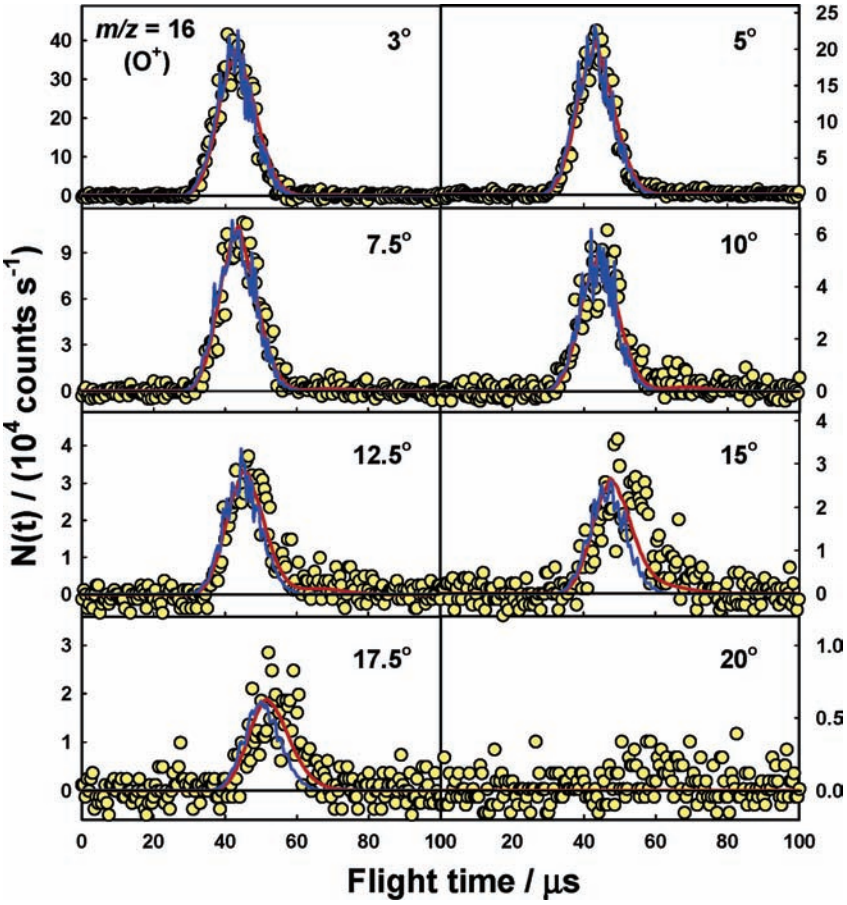

Figure 10. Time-of-flight distributions of inelastically scattered O following collisions with D_2 at $\langle E_{coll} \rangle = 24.8$ kcal mol^{-1}. The circles are the experimental data. The blue and red solid curves are the forward-convolution simulations of the data, derived from the c.m. angular and translational energy distributions of corresponding colors in Figures 12a,b and 13a,b.

collected was based on the Newton diagram shown in Figure 1 and varied for detected masses. Signals for $m/z = 16$ (O^+) were detected at laboratory angles from 3° to 20°. Signals for $m/z = 32$ (O_2^+), used to correct the $m/z = 16$ data for the contribution of cracking of O_2 to O^+ in the ionizer, were detected from 3° to 10° (O_2 does not scatter appreciably to larger angles). We determined that the O_2 signal that is detected at $m/z = 16$ as O^+ is 11% of the O_2 signal detected at $m/z = 32$ as O_2^+. Reactive product signals were detected only at $m/z = 18$ (OD^+) and at laboratory angles of 3° to 12.5°. Counting times per angle varied from 12.5 min for collection of the $m/z = 16$ and 32 data to 1.4 h for $m/z = 18$.

The nominal velocity of the O_2 component of the hyperthermal beam is the same as that of the oxygen-atom component, so the nominal c.m. collision energy of O_2 with D_2 is greater than the $O + D_2$ collision energy by the ratio of reduced masses, or 1.11. Nevertheless, the molecular oxygen present in the hyperthermal oxygen beam has no bearing on the observed scattering distributions. For the inelastic scattering signals, TOF distributions were collected for both O and O_2, and any cracking of O_2 in the ionizer to O^+ was subtracted from the $m/z = 16$ (O^+) TOF distributions. The presence of O_2 therefore would not affect the results for the inelastic scattering. Regarding the reactive scattering to form OD, the lowest barrier reaction in which O_2 can lead to signal at $m/z = 18$ (OD^+) is $O_2(^3\Sigma) + D_2 \rightarrow OOD + D$, where the OOD cracks to OD in the ionizer. The endoergicity of this reaction, however, is ~55 kcal mol^{-1}, which is much larger than the available energy. Thus, this reaction cannot occur, and we can reasonably rule out any interference of O_2 on the observed OD reactive signal.

B. Results. Laboratory TOF and angular distributions were collected for $m/z = 16$ (O^+), 18 (OD^+), and 32 (O_2^+) at an average collision energy, $\langle E_{coll} \rangle$, of 24.8 kcal mol^{-1}. The Newton diagram in Figure 1 shows the maximum recoil velocities of O and OD, given the nominal available energy. For inelastic scattering of oxygen atoms, the available energy is the collision energy. However, for reactive scattering to form OD, the maximum energy available for translation is the collision energy minus the endoergicity of the reaction (24.8 − 1.93 kcal mol^{-1}), or 22.87 kcal mol^{-1}.[46] Scattered O_2 is not included in the Newton diagram because the only purpose for its collection was to correct for its contribution (from dissociative ionization) to the TOF distributions detected at $m/z = 16$.

1. Inelastic Scattering. Figure 10 shows TOF distributions for $m/z = 16$ collected at six laboratory angles. The TOF distributions at 3°−10° (where signal was observed for $m/z = 32$) were corrected for the contribution of O_2 cracking to O^+ in the ionizer. The laboratory angular distribution for oxygen-atom inelastic scattering is shown in both panels in Figure 11. The blue and red solid curves in both Figures 10 and 11 are the forward-convolution simulations to the data, based on the corresponding blue and red c.m. translational energy and angular distributions in Figures 12 and 13. These figures illustrate the range of uncertainty in the derivation of the $P(E_T)$ and $T(\theta)$ distributions for inelastic scattering. Both the narrow and broad $P(E_T)$ distributions, shown in Figure 12, parts a and b, respectively, can be paired with the corresponding $T(\theta)$ distributions in Figure 13, parts a and b, to predict acceptable fits to the laboratory data in Figures 10 and 11. The narrower translational energy and angular distributions, seen in Figures

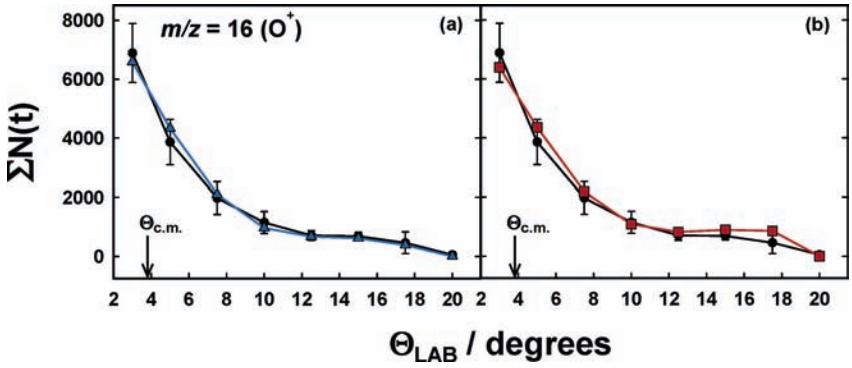

Figure 11. Laboratory angular distributions of O atoms which scattered inelastically from D_2 with $\langle E_{coll} \rangle = 24.8$ kcal mol^{-1}. The black symbols with error bars are the experimental data, and the line-connected colored symbols are the forward-convolution fits to the data, derived from the c.m. angular and translational energy distributions of corresponding color in Figures 12 and 13. The error bars are estimated from fitting the experimental TOF distributions with a modified Gaussian function and finding maximum and minimum acceptable fits by adjusting the Gaussian parameters. The integrated ranges of these fits are shown as error bars.

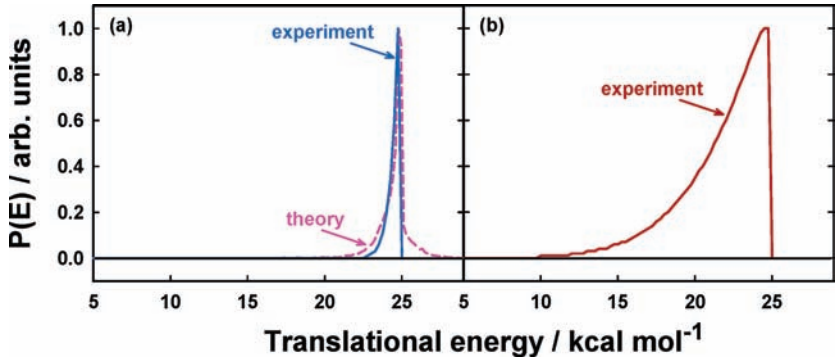

Figure 12. Center-of-mass translational energy distributions for the inelastic scattering of O from D_2 at $\langle E_{coll} \rangle = 24.8$ kcal mol^{-1}, used in the forward-convolution fit of the laboratory TOF and angular distributions for $m/z = 16$ (O^+). The blue and red curves show the limiting distributions which gave acceptable fits to the data (when paired with the curves of corresponding color in Figure 13). The dashed curve in panel (a) is the result from a QCT calculation where trajectories with scattering angles smaller than 15° were discarded.

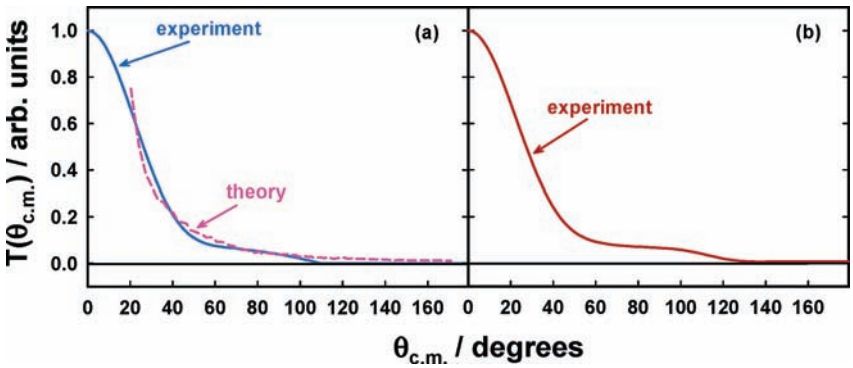

Figure 13. Center-of-mass angular distributions for O atoms that scattered inelastically from D_2 at $\langle E_{coll} \rangle = 24.8$ kcal mol^{-1}, used in the forward-convolution fit to the laboratory TOF and angular distributions for $m/z = 16$ (O^+). The blue and red curves show the limiting distributions which gave acceptable fits to the data (when paired with the curves of corresponding color in Figure 12). The dashed curve in panel (a) is the result from a QCT calculation where trajectories with scattering angles smaller than 15° were discarded.

12a and 13a, are similar to QCT results for $O(^3P) + D_2 \rightarrow O(^3P) + D_2$ scattering at $E_{coll} = 25$ kcal mol^{-1}, which are shown as dashed curves in these figures. Both experimental and theoretical translational energy distributions have maxima near the available energy and angular distributions that peak at $\theta = 0°$ (forward-scattering of O atoms). And given the uncertainty in the experimentally derived distributions, the shapes of the experimental and theoretical translational energy and angular distributions may be considered to be the same. The QCT calculations were run on analytical potential energy surfaces (PESs) for the $^3A'$ and $^3A''$ states developed by Rogers et al. for the reaction of $O(^3P)$ with H_2,[5] and c.m. translational energy and angular distributions were extracted from the trajectory data. Both the $^3A'$ and $^3A''$ surfaces gave nearly identical results for inelastic scattering. To establish a fair comparison with experiments, the QCT product energy and angular distributions have been calculated using trajectories in which the scattering angle is larger than 15°. The reason for this is that the minimum experimental laboratory angle of 3° corresponds to a c.m. angle (deflection angle) of 15°. Thus, although our fit to the time-of-flight measurements using the forward-convolution method generates global product translational energy and angular distributions, the method is not sensitive to the forward-scattering region. The consequence of the optimization can be seen in the experimental c.m. angular distribution in Figure 13. Whereas one would expect a sharp forward peak in the

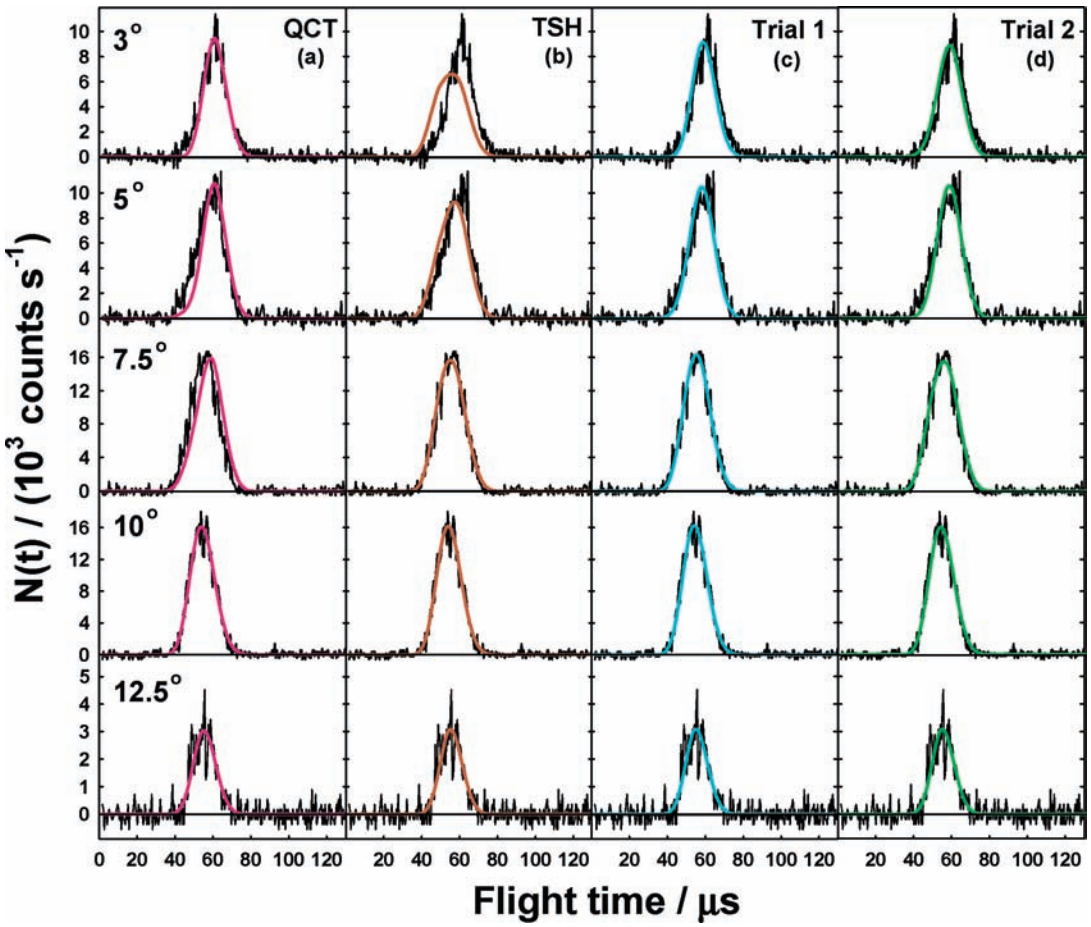

Figure 14. Each column contains the experimental time-of-flight distributions (black curves) for reactively scattered OD (detected at $m/z = 18$) following reaction of $O(^3P)$ with D_2 at $\langle E_{coll} \rangle = 24.8$ kcal mol^{-1}. The angles shown in each panel refer to the laboratory angles, Θ_{LAB}, where the data were collected. The colored curves in each column, (a), (b), (c), (d), are the forward-convolution simulations of the data, derived from the c.m. angular and translational energy distributions of corresponding color in Figures 16a−d and 17a−d, respectively.

experimental distributions due to the presence of elastic scattering, the intensity of this experimental angular distribution bends over to an asymptotic value at small scattering angles. The shape in the experimentally derived c.m. angular distribution is the result of extrapolation to $\theta = 0°$ with the Legendre function.

The major differences between the c.m. distributions derived from the experimental data and the QCT results for both surfaces are in the widths of the two distributions. The QCT results show that the translational energy distribution is very narrow and falls to zero (on the low-energy side) near 22 kcal mol^{-1}, whereas the experimental result only provides a range of uncertainty in the width of the translational energy distribution. The angular distribution also falls (at larger angles) somewhat more sharply in the QCT calculations than in the experimental distribution. The general results from the QCT calculations and the experimentally derived distributions are the same, showing forward-scattering of the oxygen atoms, with very little energy transferred into the D_2 collision partner. The simulation provides good agreement with the data in Figures 12 and 13, falling within the uncertainty range of the experimental results. As discussed in the previous section, the limited velocity resolution of the data results in simulated "fits" that are not entirely unique. Small changes in the c.m. translational energy and angular distributions will still result in acceptable fits to the data. As can be seen, the translational energy distribution for the inelastic scattering of O from D_2 can be broadened slightly, while keeping the peak near 25 kcal mol^{-1}, and the fit to the laboratory TOF and angular distributions is not greatly affected. On the other hand, large changes, altering the character of the generated c.m. distributions, show significant deviations from the simulated results. Although the velocity resolution is lower than would be desired, the data still lead essentially to the same conclusions about the inelastic scattering dynamics as do the theoretical calculations.

2. Reactive Scattering. Representative TOF distributions of the only reactively scattered product observed, OD, collected at laboratory angles of 3°, 5°, 7.5°, 10°, and 12.5°, are shown in black in each column in Figure 14. The distributions at 3°, 5°, and 7.5° had to be corrected for the contribution of ^{18}O atoms that scattered inelastically from D_2. This correction was accomplished by multiplying the scattering signal at $m/z = 16$ (O^+) for each angle by 0.002 (0.2% ^{18}O, which was measured by scattering atomic oxygen from helium and observing the scattered signal at $m/z = 16$ (O^+) and $m/z = 18$ ($^{18}O^+$) in a separate experiment), shifting by the appropriate ion flight time difference, and subtracting it from the TOF distributions collected at $m/z = 18$. This correction was negligible (less than one count) at angles greater than 7.5°, and so these angles were not corrected for ^{18}O contributions. The laboratory angular distribution is shown in black in each panel of Figure 15.

The relatively poor velocity and angular resolution of the data made it difficult to derive unique c.m. angular and translational energy distributions, but the theoretical calculations helped guide the analysis. Center-of-mass angular and translational energy distributions for the $O(^3P) + D_2 \rightarrow OD + D$ reaction were obtained from the QCT calculations. The symbols and dashed

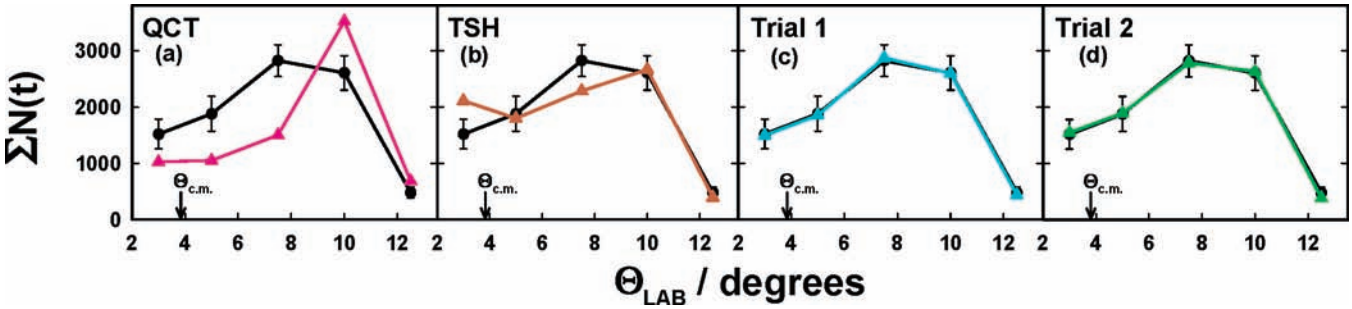

Figure 15. Each panel contains the laboratory angular distribution (black symbols with error bars) of the OD product from the reaction of $O(^3P)$ with D_2 at $\langle E_{coll} \rangle = 24.8$ kcal mol^{-1}. The error bars are estimated from fitting the TOF distributions with a modified Gaussian function and finding maximum and minimum acceptable fits by adjusting the Gaussian parameters. The integrated ranges of these fits are shown as error bars. The colored curves in each panel, (a), (b), (c), and (d), are the forward-convolution simulations to the data, derived from the c.m. angular and translational energy distributions of corresponding color in Figures 16a−d and 17a−d, respectively.

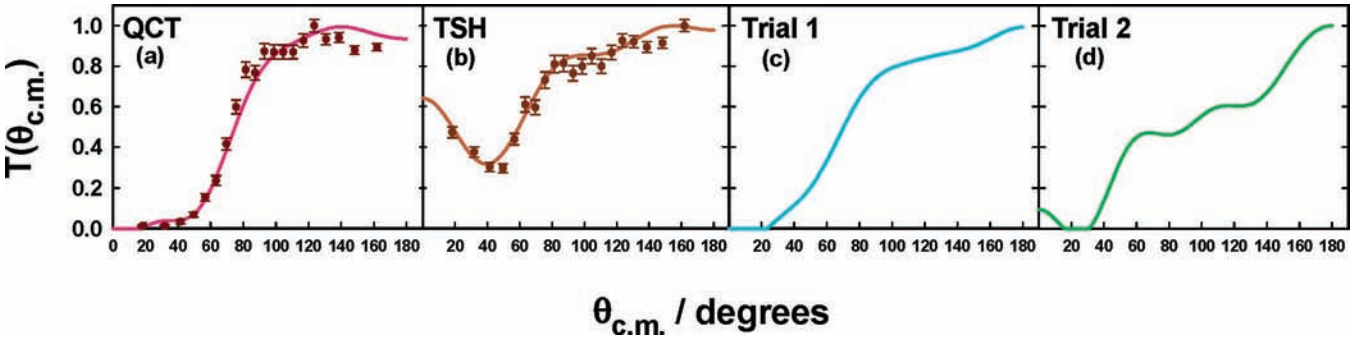

Figure 16. Center-of-mass angular distributions for the OD product of the $O(^3P) + D_2 \rightarrow OD + D$ reaction. (a) Symbols with error bars: distribution from QCT calculations, assuming reaction only on the two low-lying reactive triplet surfaces, $^3A'$ and $^3A''$. Solid curve: fit to calculated points from sum of Legendre polynomials. (b) Symbols with error bars: distribution from trajectory-surface-hopping calculations (TSH). Solid curve: fit to calculated points from sum of Legendre polynomials. (c) "Trial 1" distribution, which when paired with the translational energy distribution in Figure 17c, produces acceptable fits to the data. (d) "Trial 2" distribution, which, when paired with the translational energy distribution in Figure 17d, produces acceptable fits to the data.

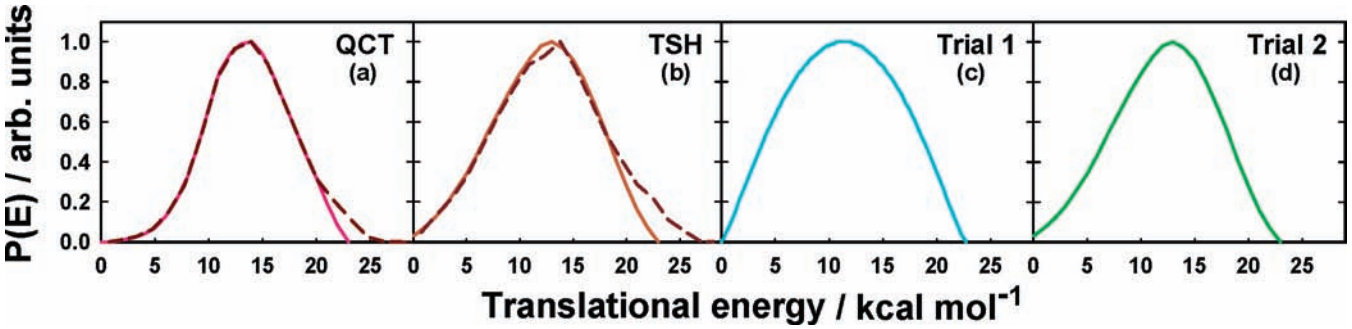

Figure 17. Center-of-mass translational energy distributions for the $O(^3P) + D_2 \rightarrow OD + D$ reaction. (a) The dashed curve is the distribution from QCT calculations, assuming reaction only on the two low-lying reactive triplet surfaces, $^3A'$ and $^3A''$. The distribution used for the forward-convolution analysis was corrected (solid curve) such that it goes to zero at the available energy. (b) The dashed curve is the distribution from trajectory-surface-hopping calculations (TSH). The distribution used for the forward-convolution analysis was corrected (solid curve) such that it goes to zero at the available energy. (c) "Trial 1" distribution, which, when paired with the angular distribution in Figure 16c, produces acceptable fits to the data. (d) "Trial 2" distribution, which, when paired with the angular distribution in Figure 16d, produces acceptable fits to the data.

curve in Figures 16a and 17a, respectively, are the results of the single surface QCT calculations described earlier (see section IIA and Figures 4 and 5). These c.m. distributions were used in the forward-convolution procedure to predict laboratory TOF and angular distributions. But before using these c.m. distributions, they were modified slightly. The calculated c.m. angular distribution was fit with a sum of eleven Legendre polynomials, which is shown as the solid, red curve in Figure 16a. The calculated translational energy distribution shown in Figure 17a has a high-energy tail that extends beyond the available energy, as a result of zero-point energy in the QCT calculations, so it was modified (solid curve) such that it went to zero at the available energy. Forward convolution of the modified c.m. distributions gave predicted TOF and laboratory angular distributions shown as red curves in Figures 14a and 15a. The TOF distributions are fit fairly well, although there is some discrepancy with the TOF data at $\Theta_{LAB} = 5°$ and 7.5°, but the predicted laboratory angular distribution is a very poor match to the experimental distribution. This poor match between the prediction of the triplet-only QCT calculations and the data suggests the possibility that intersystem crossing might be playing a role in the reaction. This possibility was investigated by using the c.m. angular and translational energy distributions obtained from the TSH calculations (Figures 16b and 17b) to predict the laboratory TOF and angular distributions (Figures 14b and 15b). For the forward-convolution calculation, the TSH angular

distribution was fit with a sum of eight Legendre polynomials, and the TSH translational energy distribution was modified such that the high-energy tail went to zero at the available energy. The predicted TOF distributions (Figure 14b) do not agree with the data for small laboratory angles, and the predicted laboratory angular distribution, while matching the data better than the prediction of the QCT results, still does not agree within the error limits of the data. Given the small but statistically significant discrepancy between the TSH prediction and the data, it appears that either intersystem crossing is not accurately described by the TSH calculations or that there are additional errors in the calculations.

Although finding unique c.m. angular and translational energy distributions is difficult given the velocity resolution of our experiment, we explored a wide range of c.m. distributions and gained a good understanding of the kinds of angular and translational energy distributions that are consistent with our data. An example of a pair of c.m. distributions that predict the observed data very well is shown in Figures 16c and 17c. This example, which we refer to as "Trial 1", illustrates a situation where the OD product is mainly backward-scattered (Figure 16c), and the shape of the angular distribution is similar to that calculated for triplet-only reactions by the QCT method (Figure 16a). However, the translational energy distribution in Figure 17c is significantly different in shape from the QCT result: it is broader and shows much more probability density at lower translational energies. A second pair of c.m. distributions ("Trial 2") that predict the data very well is presented in Figures 16d and 17d. The translational energy distribution of this trial (Figure 17d) is identical to the TSH distribution (solid curve) in Figure 17b. To obtain a good prediction of the TOF and angular data with this translational energy distribution, which is closer to both theoretical distributions than the distribution in Figure 17c, the c.m. angular distribution must have a shape that includes more forward-scattering than the QCT result in Figure 16a, with a minimum in the range $\theta = 20°-30°$ and enhanced probability density in the forward and backward directions. These two examples, Trial 1 and Trial 2, are shown to illustrate the two general conditions under which good fits to the data could be obtained. Small variations from either of these examples will still result in acceptable fits, but the trends remain unchanged. We have explored many different translational energy and angular distributions, and we have found that the data are generally consistent with either (1) a relatively broad translational energy distribution, which has high intensity at low energy, paired with a backward-peaked angular distribution, or (2) a narrower translational energy distribution, with a higher-energy peak, paired with a broader and mildly forward−backward-peaked angular distribution. Combinations of translational energy and angular distributions that are qualitatively different from those presented as Trial 1 and Trial 2 do not yield reasonable fits to the data.

Velocity−flux maps created from the four different sets of translational energy and angular distributions from Figures 16 and 17 are shown in Figure 18. These show trends that reflect what we have already discussed, with panels (b) and (d) showing a small forward-scattering peak that presumably arises from ISC. We can draw several general conclusions about the scattering on the basis of this analysis. All c.m. angular distributions show a preponderance of backward-scattering. The presence of forward-scattered OD is likely, although it is difficult to determine quantitatively. We can also conclude that there is a broad range of energy transferred into the recoiling OD fragment, and on average, about 50% of the available energy

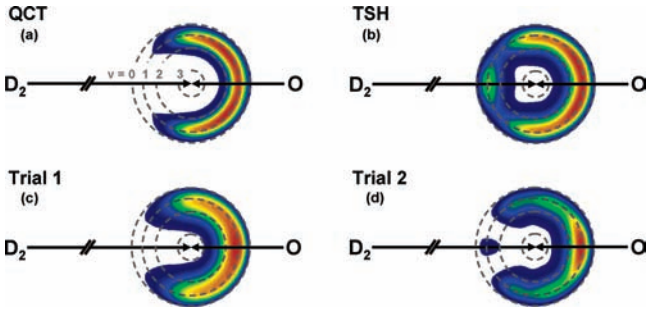

Figure 18. Center-of-mass velocity−flux maps for the OD product, derived from the four pairs of angular and translational energy distributions shown in Figures 16a−d and 17a−d. The radii of the dashed circles indicate the maximum possible OD velocities when OD is produced in vibrational states, $v = 0, 1, 2, 3$.

for reaction ($E_{coll} - \Delta E_r$) goes into internal energy of the OD. Of the four sets of c.m. distributions that we used to interpret the laboratory angular and velocity distributions, set (a), which is based on single-surface QCT results, gives the poorest fit to the data. Set (c) predicts the data well, but is not consistent with theory. Set (b) is reasonably consistent with the data and matches the theory accurately, while set (d) is a better match to the data but a poorer match to theory than (b). The results for sets (b) and (d) are similar, and they differ significantly from sets (a) and (c), showing that we have sufficient precision in the comparison between theory and experiment to conclude that ISC effects play a noticeable, though minor, role in the dynamics.

IV. Discussion

The experimental results show that inelastic and reactive scattering events resulting from collisions of $O(^3P)$ with D_2 exhibit significantly different dynamics. For both the inelastic and reactive scattering experiments, these results have been compared with high-quality triplet-only QCT calculations, and for the reactive results we have also studied quantum scattering and trajectory-surface-hopping multiple surface dynamics. From the theory, experiments, and the comparison of the two, we are able to develop a consistent interpretation of the data.

In the case of inelastic scattering, the experimental results showed that oxygen atoms scatter from D_2 with little change in direction and translational energy. The c.m. translational energy distribution for the oxygen atoms has a maximum near the c.m. collision energy in both the experimental and QCT results, implying little internal energy transfer. It appears that in a small fraction of the inelastic collisions, some of the energy in the collision may be transferred into internal energy of the D_2, but this quantity is estimated to be always less than ~20% of the collision energy. As expected, the c.m. angular distribution derived from the experimental data for the inelastic scattering of O has the highest probability density in the direction of the reagent oxygen atoms, which is in agreement with the results of the QCT calculations. In addition, the experimentally derived translational energy distribution has a maximum at the collision energy and may be very narrow, again in close agreement with the results of the QCT calculations. We can thus conclude that, within our experimental error, the QCT calculations reproduce the experimental findings, and in both experiment and theory, the picture of scattering that emerges is one in which oxygen atoms scatter from D_2 molecules with large-impact-parameter ("glancing") collisions, resulting in very little energy transfer into the D_2 molecule and very little change in direction.

Reactive scattering of OD was clearly observed in the experiments, but the limited velocity resolution of the data made

it challenging to derive precise c.m. translational energy and angular distributions. The QCT calculations, which do not include coupling to the singlet surfaces, provided a starting point in the forward-convolution approach to the data analysis. The match to the data was marginally acceptable for the TOF distributions but unacceptable for the laboratory angular distribution. The poor agreement between the triplet-only QCT calculations and the experimental results suggested the possibility that intersystem crossing is important in the $O(^3P) + D_2$ reaction. Therefore, we compared the prediction of the TSH calculations with the data. The agreement with the data was improved but not within the experimental uncertainty. Many different c.m. angular and translational energy distributions were therefore investigated in order to find c.m distributions which accurately predict the laboratory TOF and angular distributions and to test the sensitivity of the laboratory distributions to the assumed c.m. distributions. Although there are many possible sets of c.m. angular and translational energy distributions which provide good fits to the laboratory TOF and angular distributions, there are two general categories of behavior which are exemplified by the results referred to as Trial 1 and Trial 2. Trial 1 shows a purely backward-scattered angular distribution and a translational energy distribution with considerable intensity at low translational energy. Trial 2 shows some forward-scattering and less intensity at low translational energy. Although the analysis demonstrates the difficulty of deriving unique c.m. distributions from the experimental data, Trial 2 is reasonably close to the TSH results (the translational distribution matches exactly, and the angular distribution shows somewhat less forward-scattering and more backward-scattering), and thus is the preferred fit.

The importance of quantum effects in this reaction involving light atoms needs to be carefully assessed, as they could be a source of discrepancy between theory and experiment. For the single-surface results, Figure 4 shows good agreement between QCT and accurate quantum results, so differences between theory and experiment cannot be due to quantum effects in this case. The situation is less clear concerning the multiple-surface results. A recent multisurface quantum scattering calculation[48] (for $O + H_2$) based on the same Hamiltonian that we have used in the TSH calculations produced integral cross sections that were qualitatively similar to TSH results.[27] However, there were differences of up to a factor of 2 for the integral cross sections (associated with spin-forbidden products), with the TSH calculations yielding higher cross sections at higher energy, so it is clear that the comparison is not quantitative. Unfortunately, no information concerning product translational energy or angular distributions was available from the quantum calculations, so it is not possible to provide a more detailed estimate of what changes in these distributions might result from quantum effects. In the comparison with the Trial 2 angular distribution, the TSH calculation appears to overestimate the forward intensity, which is consistent with the result just noted that the TSH cross section overestimates ISC at high energy. Indeed, the results of Trial 2 suggest that a better fit to experiment is provided by angular distributions that have a smaller forward component. It thus appears that ISC has a noticeable effect on the results but is probably not as important as is suggested by the TSH calculations.

Under any interpretation of the analysis, the OD is largely backward-scattered, which is consistent with reaction mainly on the $^3A'$ and $^3A''$ diabats. The data analysis also shows that an average of ~50% of the available energy goes into internal energy of the OD fragment, in agreement with the results of all the theoretical calculations. The nature of the OD scattering dynamics, predominantly backward-scattered with large internal excitation, is indicative of a small-impact-parameter ("head-on") collision between the O and D_2. The microscopic mechanism giving rise to such dynamics is often termed a "rebound mechanism."[49] The prominent backward-scattering and large energy transfer stand in stark contrast to the inelastic scattering dynamics which showed exclusive forward-scattering with very little energy transfer.

In our experiments, it is impossible to tell how the energy is partitioned into vibration and rotation; however, the partitioning of internal energy has been addressed in QCT calculations by Braunstein and Schatz,[25] and the present CCH results in Figure 3 are consistent with those earlier results. Braunstein and Schatz found that in the reaction, $O(^3P) + H_2(v = 0) \rightarrow OH(v', j') + H$, at $E_{coll} = 26$ kcal mol^{-1}, the $v' = 0$ state of the OH is the most populated, followed by small populations in the $v' = 1$ and 2. There was no population in vibrational states above $v' = 2$ when the H_2 reactant was in the ground vibrational state. Rotational distributions calculated for reaction at $E_{coll} = 18$ kcal mol^{-1} showed rotational population up to the $j' = 16$ state of OH, with a peak around $j' = 6$ for the $v' = 0$ state. For $O(^3P) + D_2(v = 0) \rightarrow OD(v', j') + D$ at $E_{coll} = 25$ kcal mol^{-1}, we find that most of the OD molecules are also vibrationally cold, with about 30% of the population in $v' = 1$, and less than 5% of the population in higher states. The $v' = 0$ rotational populations peak in $j' = 15$. These results indicate that the energy transferred to internal degrees of freedom of the OH and OD products in the $O(^3P) + H_2/D_2$ reactions goes into both vibration and rotation.

One possible source of discrepancy between theory and experiment is errors in the potential energy surfaces. The ab-initio calculations used for the Rogers et al.[5] surfaces are of very high quality, and it seems likely that the highest-level calculations they used are good to better than 1 kcal mol^{-1}. Indeed, a recent reevaluation of the OH bond dissociation energy[47] leads to an even smaller error in the reaction endoergicity than was originally surmised. Errors in the potential energy surfaces due to fitting errors could be much more important, and if these were to cause excess repulsion between the departing products, they could easily produce the observed difference between theoretical and experimental results. Rogers et al.[5] provided detailed information about their fitting errors; however, they did not indicate the energy range or geometries of the 951 ab-initio points (112 for high-quality calculations) that were used in determining the fit, so we do not have sufficient information available to quantitatively assess the accuracy of their surfaces as it relates to our application. Most likely the energies of interest in the present study are higher than they considered, which means that fitting errors could play a role in the differences between theory and experiment.

V. Concluding Remarks

The dynamics of the interactions of $O(^3P)$ with D_2 have been investigated in detail with crossed-molecular-beams methods and with various theoretical calculations. Experiments on the inelastic scattering of $O(^3P) + D_2$ show that oxygen atoms scatter from D_2 in relatively large-impact-parameter collisions leading to forward-scattering with very little internal energy transfer to D_2. In contrast, the only reactive channel, $O(^3P) + D_2 \rightarrow OD + D$, gave OD products that were predominately backward-scattered and had a relatively large internal excitation (~50% of the available energy). The scattering behavior of the OD was thus indicative of small-impact-parameter collisions

between the two reactants. All of the dynamics observed in the experiments were in good qualitative agreement with single-surface quasiclassical trajectory calculations; however, a careful analysis reveals noticeable differences. The presence of intersystem crossing was investigated, and the comparison between theory and experiment suggests that intersystem crossing is a measurable but minor process that results in lower-translational-energy products and some forward-scattering of OD. Unfortunately, uncertainties in the experimental results and possible quantum effects in the theory are such that the intersystem crossing probability cannot be determined accurately. Although the potential surfaces are based on very high quality ab-initio calculations, it is also possible that errors in the fitting of these calculations could account for the remaining discrepancies between theory and experiment.

Acknowledgment. This work was supported by grants from the Department of Defense Experimental Program for the Stimulation of Competitive Research (DEPSCoR), administered by the Air Force Office of Scientific Research (Grant Nos. F49620-01-1-0276 and FA9550-04-1-0428), from the Air Force Office of Scientific Research through a Multidisciplinary University Research Initiative (Grant No. F49620-01-1-0335), and from the National Science Foundation (CHE-0131998).

References and Notes

(1) Garton, D. J.; Minton, T. K.; Maiti, B.; Troya, D.; Schatz, G. C. *J. Chem. Phys.* **2003**, *118*, 1585.

(2) Sultanov, R. A.; Balakrishnan, N. *J. Chem. Phys.* **2004**, *121*, 11038.

(3) Balakrishnan, N. *J. Chem. Phys.* **2004**, *121*, 6346.

(4) Balakrishnan, N. *J. Chem. Phys.* **2003**, *119*, 195.

(5) Rogers, S.; Wang, D.; Kuppermann, A.; Walch, S. P. *J. Phys. Chem. A* **2000**, *104*, 2308.

(6) Chatfield, D. C.; Friedman, R. S.; Lynch, G. C.; Truhlar, D. G.; Schwenke, D. W. *J. Chem. Phys.* **1993**, *98*, 342.

(7) Joseph, T.; Truhlar, D. G.; Garrett, B. C. *J. Chem. Phys.* **1988**, *88*, 6982.

(8) Bowman, J. M. *Chem. Phys. Lett.* **1987**, *141*, 545.

(9) Wagner, A. F.; Bowman, J. M. *J. Chem. Phys.* **1987**, *86*, 1976.

(10) Garrett, B. C.; Truhlar, D. G. *Int. J. Quantum Chem.* **1986**, *29*, 1463.

(11) Garrett, B. C.; Truhlar, D. G.; Schatz, G. C. *J. Am. Chem. Soc.* **1986**, *108*, 2876.

(12) Schatz, G. C. *J. Chem. Phys.* **1985**, *83*, 5677.

(13) Wright, J. S.; Donaldson, D. J.; Williams, R. J. *J. Chem. Phys.* **1984**, *81*, 397.

(14) Walch, S. P.; Dunning, T. H.; Raffenetti, R.; Bobrowicz, F. W. *J. Chem. Phys.* **1980**, *72*, 406.

(15) Howard, R. E.; McLean, A. D.; Lester, W. A. *J. Chem. Phys.* **1979**, *71*, 2412.

(16) Schinke, R.; Lester, W. A. *J. Chem. Phys.* **1979**, *70*, 4893.

(17) Johnson, B. R.; Winter, N. W. *J. Chem. Phys.* **1977**, *66*, 4116.

(18) Han, J.; Chen, X.; Weiner, B. R. *Chem. Phys. Lett.* **2000**, *332*, 243.

(19) Alagia, M.; Balucani, N.; Cartechini, L.; Casavecchia, P.; van Kleef, E. H.; Volpi, G. G.; Kuntz, P. J.; Sloan, J. J. *J. Chem. Phys.* **1998**, *108*, 6698.

(20) Davidson, J. A.; Schiff, H. I.; Streit, G. E.; McAfee, J. R.; Schmeltekopf, A. L.; Howard, C. J. *J. Chem. Phys.* **1977**, *67*, 5021.

(21) Gary, S. K.; Balint-Kurti, G. G.; Schatz, G. C.; Lin, J. J.; Liu, X.; Harich, S.; Yang, X. *J. Chem. Phys.* **2000**, *113*, 7330.

(22) Liu, X. H.; Lin, J. J.; Harich, S.; Schatz, G. C.; Yang, X. *Science* **2000**, *289*, 1536.

(23) Aoiz, F. J.; Banares, L.; Castillo, J. F.; Brouard, M.; Denzer, W.; Vallance, C.; Honvault, P.; Launay, J.-M.; Dobbyn, A. J.; Knowles, P. J. *Phys. Rev. Lett.* **2001**, *86*, 1729.

(24) Schatz, G. C.; Pederson, L. A.; Kuntz, P. J. *Faraday Discuss.* **1997**, *108*, 357.

(25) Braunstein, M.; Alder-Golden, S.; Maiti, B.; Schatz, G. C. *J. Chem. Phys.* **2004**, *120*, 4316.

(26) Hoffman, M. R.; Schatz, G. C. *J. Chem. Phys.* **2000**, *113*, 9456.

(27) Maiti, B.; Schatz, G. C. *J. Chem. Phys.* **2003**, *119*, 12360.

(28) Alagia, M.; Balucani, N.; Cartechini, L.; Casavecchia, P.; van Beek, M.; Volpi, G. G.; Bonnet, L.; Rayez, J. C. *Faraday Discuss.* **1999**, *113*, 133.

(29) Rudlich, Y.; Lifson, S.; Naaman, R. *J. Chem. Phys.* **1993**, *98*, 2936.

(30) Paz, Y.; Trakhtenberg, S.; Naaman, R. *J. Phys. Chem.* **1993**, *97*, 9075.

(31) Scouteries, D.; Castilo, J. F.; Manolopoulos, D. E. *Comput. Phys. Commun.* **2000**, *133*, 128.

(32) Dobbyn, A. J.; Knowles, P. J. *Faraday Discuss. Chem. Soc.* **1998**, *110*, 247.

(33) Brunsvold, A. L.; Garton, D. J.; Minton, T. K.; Troya, D.; Schatz, G. C. *J. Chem. Phys.* **2004**, *121*, 11702.

(34) Braunstein, M.; Brunsvold, A. L.; Garton, D. J.; Minton, T. K. *J. Chem. Phys.* **2004**, *120*, 2238.

(35) Brink, G. O. *Rev. Sci. Instrum.* **1966**, *37*, 857.

(36) Daly, N. R. *Rev. Sci. Instrum.* **1960**, *31*, 264.

(37) Caledonia, G. E.; Krech, R. H.; Green, B. D. *AIAA J.* **1987**, *25*, 59.

(38) Caledonia, G. E.; Krech, R. H.; Green, B. D.; Pirri, A. N. "Source of High Flux Energetic Atoms," Physical Sciences, Inc., U.S. Patent No. 4,894,511, 1990.

(39) Proch, D.; Trickl, T. *Rev. Sci. Instrum.* **1989**, *60*, 713.

(40) Steinfeld, J. I.; Francisco, J. S.; Hase, W. L. *Chemical Kinetics and Dynamics*, 2nd ed.; Prentice Hall: New York, 1999.

(41) Houston, P. *Chemical Kinetics and Reaction Dynamics*; McGraw-Hill: Boston, 2001.

(42) Lee, Y. T. Reactive Scattering I: Nonoptical Methods. In *Atomic and Molecular Beam Methods*; Scoles, G., Ed.; Oxford University Press: New York, 1988; Vol. 1, pp 553−568.

(43) Buss, R. J. Ph.D. Thesis, University of California, Berkeley, 1979.

(44) Zhao, X. Ph.D. Thesis, University of California, Berkeley, 1988.

(45) Zhang, J. Ph.D. Thesis, Montana State University, Bozeman, 2001.

(46) The endoergicity is based on the enthalpies of formation, $\Delta H^\circ_{f,0}$, for OD and D, reported in Qian, X.-M.; Song, Y.; Lau, K.-C.; Ng, C.-Y.; Liu, J.; Chen, W.; He, G. Z. *Chem. Phys. Lett.* **2002**, *353*, 19, and for O, reported in Chase, M. W., et al. *JANAF Thermochemical Tables*, 3rd ed.; *J. Phys. Chem. Ref. Data* **1985**, *14*, Supplement No. 1.

(47) Ruscic, B.; Wagner, A. F.; Harding, L. B.; Asher, R. L.; Feller, D.; Dixon, D. A.; Peterson, K. A.; Song, Y.; Qian, X.; Ng, C. Y.; Liu, J.; Chen, W.; Schwenke, D. W. *J. Phys. Chem. A* **2002**, *106*, 2727.

(48) Chu, T. S.; Zhang, X.; Han, K. L. *J. Chem. Phys.* **2005**, *122*, 214301.

(49) Levine, R. D.; Bernstein, R. B. *Molecular Reaction Dynamics and Chemical Reactivity*; Oxford University Press: New York, 1987.